

# Nonlinear travelling periodic waves for the Euler equations in three-layer flows

Xin Guan<sup>1,†</sup>, Alex Doak<sup>2</sup>, Paul Milewski<sup>2,3</sup> and Jean-Marc Vanden-Broeck<sup>1</sup>

<sup>1</sup>Department of Mathematics, University College London, London WC1E 6BT, UK

<sup>2</sup>Department of Mathematical Sciences, University of Bath, Bath BA2 7AY, UK

<sup>3</sup>Department of Mathematics, Penn State University, Pennsylvania 16802, USA

(Received 19 September 2023; revised 16 January 2024; accepted 16 January 2024)

In this paper, we investigate periodic travelling waves in a three-layer system with the rigid-lid assumption. Solutions are recovered numerically using a boundary integral method. We consider the case where the density difference between the layers is small (i.e. a weakly stratified fluid). We consider the system both with and without the Boussinesq assumption to explore the effect the assumption has on the solution space. Periodic solutions of both mode-1 and mode-2 are found, and their bifurcation structure and limiting configurations are described in detail. Similarities are found with the two-layer case, where large-amplitude solutions are found to overhang with an internal angle of  $120^\circ$ . However, the addition of a second interface results in a richer bifurcation space, in part due to the existence of mode-2 waves and their resonance with mode-1 waves. New limiting profiles are found.

**Key words:** waves/free-surface flows

## 1. Introduction

Layered models are often used to approximate a stratified fluid with regions of almost constant density and sharp pycnoclines. This simplifies the mathematical description of the model, but results in shear instabilities in time-dependent simulations. Nonetheless, the study of steady travelling waves in layered models has proven useful in exploring wave properties in continuously stratified media which the layered models approximate (see, for example, the discussion by Ostrovsky & Stepanyants (2005) concerning the validity of two-layer models, and likewise the agreement found by Lamb (2000) between finite thickness and infinitesimally thin pycnoclines for the three-layer system). Furthermore, in cases where the upper layer is bounded above by a passive gas, the upper boundary is often replaced by a solid wall, known as the rigid-lid approximation. The work of Evans &

† Email address for correspondence: [xin.guan.20@ucl.ac.uk](mailto:xin.guan.20@ucl.ac.uk)

Ford (1996) found this approximation had small effects on the wave properties of travelling internal modes.

For layered internal wave models, previous literature focuses primarily on a two-layer fluid. Two-layer models admit one baroclinic mode, corresponding to mode-1 waves in the terminology for continuously stratified flows. Mode-1 solitary waves are found to bifurcate from uniform streams, and as their amplitude increases they either form an internal wavefront (Turner & Vanden-Broeck 1988) or form overhanging profiles (Grimshaw & Pullin 1986). Periodic waves were also found to overhang, and the limiting configuration of such waves was only recently found (Maklakov & Sharipov 2018). This solution is characterised by an internal angle of  $120^\circ$  inside one of the fluids, with a stagnant bubble attached. A more detailed description of the bifurcation structure was found by Guan, Vanden-Broeck & Wang (2021a), and in particular it was found that these solutions smoothly connect to a single-layer limiting Stokes wave as the density of the upper fluid goes to zero.

In this paper, we explore the global bifurcation structure of periodic three-layer internal waves. This is done numerically using a boundary integral formulation, where unknowns are parameterised in arclength of the interface, akin to Rusås & Grue (2002) and Chen & Forbes (2008). However, we express unknowns using Fourier series representations in terms of arclength (and hence achieving spectral accuracy) as opposed to using finite difference formulae to approximate derivatives. The three-layer rigid-lid model is especially interesting since the model admits two baroclinic modes, the so-called fast mode (mode-1) and the slow mode (mode-2). Some work has been done on solitary waves in this setting. Weakly nonlinear theories for three-layer flows such as the modified Korteweg–de Vries equation (Grimshaw, Pelinovsky & Talipova 1997) and Gardner equation (Kurkina *et al.* 2015) have been derived and used to model solitary waves of the system. Meanwhile, the strongly nonlinear but weakly dispersive three-layer Miyata–Choi–Camassa equations (Miyata 1988; Choi & Camassa 1999) were explored by Jo & Choi (2014) and Barros, Choi & Milewski (2020). Using a fully nonlinear theory, a detailed description of three-layer conjugate states was obtained by Lamb (2000). Fully nonlinear wave computations have been computed by previous authors, who explored both mode-1 (Rusås & Grue 2002) and mode-2 (Doak, Barros & Milewski 2022) solitary waves. Fully nonlinear mode-1 and mode-2 periodic waves have been computed (Rusås 2000; Chen & Forbes 2008). However, a detailed description of the bifurcation space is thus far lacking, and is presented below.

The Boussinesq assumption is a common assumption made in the theory of stratified flows, and is asymptotically justified when the density differences between the layers is small compared with a reference density. The Boussinesq assumption adds a symmetry into the system of equations such that, given a solution, one can obtain an additional solution with the same speed and energy by flipping the properties (depths and densities) of the upper and lower layer and replacing interface displacements with their negative value. Furthermore, with a symmetric choice of parameters (i.e. when the density difference between the upper and middle layers is equivalent to the difference between the middle and lower layers, and the depths of the upper and lower layers are equivalent), some Boussinesq solutions have an additional symmetry that the two interface displacements are mirror images (potentially with a phase shift of a half-wavelength of the wave). We refer to such solutions as having ‘upside-down’ symmetry hereafter. Note that not all solutions with such parameters have such symmetry, as discussed below. In this paper, we explore the solution space both with and without the Boussinesq assumption.

While reasonable on physical grounds, both the Boussinesq and rigid-lid assumptions do have clear structural mathematical consequences which are not often emphasised in the literature, for example the aforementioned breaking of symmetry, changes in the stability

characteristics (Barros & Choi 2011; Boonkasame & Milewski 2012; Heifetz & Mak 2015; Guha & Raj 2018) of certain flows, and a momentum paradox (Camassa *et al.* 2012).

For mode-1 Boussinesq solutions with a symmetric choice of parameters it is found that there exists an upside-down symmetric branch of solutions (with a half-wavelength phase-shift between the interfaces). Along this branch, a bifurcation point is found, and the bifurcating branch has solutions which are not upside-down symmetric. In fact, there are two branches emerging from the bifurcation point: one is obtained from the other by swapping the depths and density jumps of the upper and lower layer and replacing interface displacements with their negative value, according to the symmetry in the Boussinesq system described above. All of the solutions on these branches form overhangs, until either one or both interfaces touches itself and forms a trapped bubble, as found for two-layer solutions (Maklakov & Sharipov 2018; Guan *et al.* 2021a). Removing the Boussinesq assumption, or changing the symmetric choice of parameters, results in two distinct solution branches, in which no solutions have the upside-down symmetry.

For mode-2 solutions, the bifurcation space is more complicated. The Boussinesq upside-down symmetric branch of solutions in this case does not have a phase-shift in the interface reflections, and in fact the streamline at the mid-depth is a horizontal line running through the middle of the middle layer. In this sense, the solutions can be seen as two-layer mode-1 solutions reflected across a wall. Unlike the mode-1 upside-down symmetric branch, the branch has not one but two bifurcation points. All solution branches again terminate with overhanging profiles, although previously unseen limiting solutions are found in which two trapped bubbles are formed either side of the overhanging region. A detailed analysis of such solutions is beyond the scope of this paper. Breaking of the symmetry in the parameter choices (or removal of the Boussinesq assumption) results in three distinct branches. We also explore long mode-2 waves, in which mode-1 resonances are found. This results in additional branches of periodic solutions which bifurcate from a periodic Stokes wave, akin to the theory of Wilton ripples (Wilton 1915). As the wavelength is further increased, the solutions ultimately approach generalised solitary waves (Akylas & Grimshaw 1992; Rusås & Grue 2002; Doak *et al.* 2022).

The paper is organised as follows. In § 2, we formulate the problem, and discuss the linear theory. In § 3, we describe the numerical method. In § 4, we discuss the typical numerical results. Section 5 contains conclusions.

## 2. Mathematical formulation

Consider two-dimensional progressive waves travelling with constant speed  $c$  along two interfaces between three incompressible, inviscid and immiscible fluids layers (see the sketch in figure 1). We consider steady solutions on a background current of  $-c$ . We denote by  $h_j$  and  $\rho_j$  ( $j = 1, 2, 3$ ) the mean depths and densities in each fluid layer, where subscripts 1, 2 and 3 refer to fluid properties associated with the lower, middle and upper fluid layers, respectively. We denote the wavelength of the wave as  $\lambda$ . A Cartesian coordinate system is introduced such that the  $x$ -axis is halfway between the mean levels of the upper and lower interfaces, and the  $y$ -axis coincides with a vertical line through a wave crest/trough. We choose  $\rho_2$ ,  $h_2$  and  $c$  as the scalings of density, length and velocity, hence in the non-dimensionalised system that follows we have set  $h_2 = 1$  and  $\rho_2 = 1$ . We concentrate on solutions with mirror symmetry about the  $y$ -axis. The flows are irrotational; hence there exist potential functions  $\phi_j$  ( $j = 1, 2, 3$ ) satisfying the Laplace equation in the respective domains

$$\phi_{1,xx} + \phi_{1,yy} = 0, \quad -1/2 - h_1 < y < -1/2 + \eta^-, \quad (2.1)$$

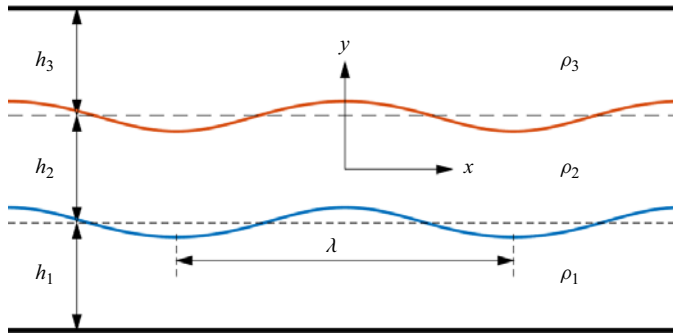


Figure 1. Schematic of the flow configuration. The dashed lines are the mean interfacial levels.

$$\phi_{2,xx} + \phi_{2,yy} = 0, \quad -1/2 + \eta^- < y < 1/2 + \eta^+, \quad (2.2)$$

$$\phi_{3,xx} + \phi_{3,yy} = 0, \quad 1/2 + \eta^+ < y < 1/2 + h_3, \quad (2.3)$$

where  $h_1$  and  $h_3$  become the non-dimensional depths of the lower and upper layers,  $\eta^-$  and  $\eta^+$  are the deviations of the lower and upper layers from their mean water levels (dashed lines in figure 1). On the interfaces, continuity of pressure gives (making use of the Bernoulli equation)

$$\phi_{2,x}^2 + \phi_{2,y}^2 - R_1(\phi_{1,x}^2 + \phi_{1,y}^2) + \frac{2(1 - R_1)}{F^2}(-1/2 + \eta^-) = B^-, \quad y = -1/2 + \eta^-, \quad (2.4)$$

$$R_3(\phi_{3,x}^2 + \phi_{3,y}^2) - \phi_{2,x}^2 - \phi_{2,y}^2 + \frac{2(R_3 - 1)}{F^2}(1/2 + \eta^+) = B^+, \quad y = 1/2 + \eta^+, \quad (2.5)$$

where  $R_1 = \rho_1/\rho_2 > 1$ ,  $R_3 = \rho_3/\rho_2 < 1$ ,  $F^2 = c^2/(gh_2)$ ,  $g$  is the acceleration due to gravity and  $B^\pm$  are the unknown Bernoulli constants. The Boussinesq approximation consists of setting  $R_1 = R_3 = 1$  only in the kinetic energy terms above. There are four kinematic boundary conditions imposed on the interfaces:

$$\phi_{1,x}\eta_x^- - \phi_{1,y} = \phi_{2,x}\eta_x^- - \phi_{2,y} = 0, \quad y = -1/2 + \eta^-, \quad (2.6)$$

$$\phi_{2,x}\eta_x^+ - \phi_{2,y} = \phi_{3,x}\eta_x^+ - \phi_{3,y} = 0, \quad y = 1/2 + \eta^+. \quad (2.7)$$

On the solid walls, we need to impose the following impermeability conditions:

$$\phi_{1,y} = 0, \quad y = -1/2 - h_1, \quad (2.8)$$

$$\phi_{3,y} = 0, \quad y = 1/2 + h_3. \quad (2.9)$$

Equations (2.1)–(2.9) complete the mathematical description of the three-layer travelling waves. There are six non-dimensional parameters:  $h_1, h_3, R_1, R_3, \lambda$  and  $F$ . Under the Boussinesq approximation, the following symmetry leaves the equations unchanged:

$$h_1 \leftrightarrow h_3, \quad R_1 - 1 \leftrightarrow -(R_3 - 1), \quad \eta^+ \leftrightarrow -\eta^-, \quad y \leftrightarrow -y. \quad (2.10)$$

Hence, for each solution found in the original system, another solution exists by reflecting the original solution about  $y = 0$  and appropriate reassignment of layer densities and heights. If, in addition,  $h_1 = h_3$  and  $R_1 - 1 = -(R_3 - 1)$ , the second solution has the same physical parameters (physical domain and density stratification) as the original one. Hence if the solution itself is not symmetric about  $y = 0$ , a new solution may be obtained this way.

2.1. Linear solutions

To obtain the dispersion relation, we consider perturbations with wavenumber  $k = 2\pi/\lambda$  of the form

$$\eta^- = \epsilon K e^{ikx} + \text{c.c.}, \quad \eta^+ = \epsilon L e^{ikx} + \text{c.c.}, \tag{2.11a,b}$$

$$\phi_1 = -x + \epsilon P \cosh(k(y + h_1 + 1/2)) e^{ikx} + \text{c.c.}, \tag{2.12}$$

$$\phi_2 = -x + \epsilon(Q \cosh(k(y + 1/2)) + S \cosh(k(y - 1/2))) e^{ikx} + \text{c.c.}, \tag{2.13}$$

$$\phi_3 = -x + \epsilon T \cosh(k(y - h_3 - 1/2)) e^{ikx} + \text{c.c.}, \tag{2.14}$$

$$B^- = (1 - R_1)(1 - 1/F^2), \quad B^+ = (R_3 - 1)(1 + 1/F^2), \tag{2.15a,b}$$

where  $K, L, P, Q, S$  and  $T$  are constant coefficients, c.c. denotes a complex conjugate and  $\epsilon$  is a small parameter to measure the nonlinearity. The  $-x$  term in the velocity potentials  $\phi_i$  corresponds to the uniform stream of speed unity, arising due to the moving frame of reference. Substituting the above quantities into (2.4)–(2.7) and collecting terms of  $O(\epsilon)$ , we can get six homogeneous linear equations for  $K, L, P, Q, S$  and  $T$ . Using the solvability condition, we can obtain a fourth-order algebraic equation of  $F$ :

$$\mathcal{A}F^4 + \mathcal{B}F^2 + \mathcal{C} = 0, \tag{2.16}$$

where the coefficients are

$$\mathcal{A} = k^2[1 + \coth(k)(R_1 \coth(kh_1) + R_3 \coth(kh_3)) + \coth(kh_1) \coth(kh_3)R_1R_3], \tag{2.17}$$

$$\mathcal{B} = k[\coth(k)(R_3 - R_1) + R_3 \coth(kh_3)(1 - R_1) - R_1 \coth(kh_1)(1 - R_3)], \tag{2.18}$$

$$\mathcal{C} = R_3 + R_1 - R_3R_1 - 1. \tag{2.19}$$

Solving this equation for the positive roots, we obtain the following two branches of the dispersion relation:

$$F_1 = c_{p1}(k, R_1, R_3, h_1, h_3), \quad F_2 = c_{p2}(k, R_1, R_3, h_1, h_3), \tag{2.20a,b}$$

where  $c_{p1} \geq c_{p2}$  for the same parameters (a rigorous proof that  $F^2 > 0$  can be found in Yih (2012), which applies to Euler multilayer fluids). Here  $c_{p1}$  and  $c_{p2}$  are the phase velocities of the mode-1 and the mode-2 waves. Mode-1 waves are defined by interface displacements of the same polarity ( $KL > 0$ ) and mode-2 waves have interface displacements of opposite polarity ( $KL < 0$ ). These linear solutions will be used as initial guesses to generate fully nonlinear profiles, and to motivate certain resonances between modes.

3. Numerical method

3.1. Boundary integral equations

For periodic waves having a wavenumber  $k$ , we introduce the following transformation:

$$\zeta = e^{-ikz}, \tag{3.1}$$

where  $z = x + iy$ . This maps the physical region in one spatial period to an annular region in the  $\zeta$ -plane and enables us to apply Cauchy’s integral formula to solve the Laplace equation. Introducing the complex velocity  $w = u - iv$ , where  $u$  and  $v$  are the horizontal

Downloaded from https://www.cambridge.org/core. IP address: 18.222.167.249, on 16 Nov 2024 at 17:23:38, subject to the Cambridge Core terms of use, available at https://www.cambridge.org/core/terms. https://doi.org/10.1017/jfm.2024.73

and vertical components of the velocity, we have the following Cauchy's integral formula on the  $\zeta$ -plane:

$$w(\zeta') = \frac{1}{i\pi} \oint_C \frac{w(\zeta)}{\zeta - \zeta'} d\zeta, \tag{3.2}$$

where  $\zeta$  and  $\zeta'$  are points on the boundary  $C$  of each fluid layer on which the integral is evaluated. Note that the integral has a singularity when  $\zeta = \zeta'$ , therefore, the integral is in the sense of Cauchy principal value. We can express the complex velocity  $w$  in terms of the velocity modulus  $q$  and the inclination angle  $\theta$  as

$$w = q e^{-i\theta}. \tag{3.3}$$

On the interface,  $\theta$  has the following relation to  $z$ :

$$\frac{dz}{ds} = e^{i\theta}, \tag{3.4}$$

where  $s$  is the physical arclength parameter and we require that  $s$  is monotonically increasing along the interfaces in the direction such that the relatively heavier fluid is always to the right of the interfaces. In this way, (3.2) can be rewritten as

$$w(s') = -\frac{k}{\pi} \oint_C \frac{q(s)}{1 - \zeta(s')/\zeta(s)} ds, \tag{3.5}$$

where we have used (3.4). For the lower and the upper layer, (3.5) requires the information on the solid walls. However, using the Schwarz reflection principle, we can avoid this by reflecting the lower (upper) interface with respect to the bottom (top) wall to get a mirror image. In this fashion, the solid boundaries become a flat streamline inside the new region of the lower and upper layer, and (3.5) can be calculated by evaluating the integral on the physical interface and its mirror image. In the lower fluid layer,

$$\zeta(s')/\zeta(s) = \begin{cases} e^{-ik(x'-x)} e^{k(\eta^{-'}-\eta^-)}, & \text{on the lower interface,} \\ e^{-ik(x'-x)} e^{k(\eta^{-'}+\eta^-+2h_1)}, & \text{on the image of lower interface;} \end{cases} \tag{3.6}$$

in the upper layer,

$$\zeta(s')/\zeta(s) = \begin{cases} e^{-ik(x'-x)} e^{k(\eta^{+'}-\eta^+)}, & \text{on the upper interface,} \\ e^{-ik(x'-x)} e^{k(\eta^{+'}+\eta^+-2h_3)}, & \text{on the image of upper interface;} \end{cases} \tag{3.7}$$

on the lower interface of the middle layer,

$$\zeta(s')/\zeta(s) = \begin{cases} e^{-ik(x'-x)} e^{k(\eta^{-'}-\eta^-)}, & \text{on the lower interface,} \\ e^{-ik(x'-x)} e^{k(\eta^{-'}-\eta^+-1)}, & \text{on the upper interface;} \end{cases} \tag{3.8}$$

on the upper interface of the middle layer,

$$\zeta(s')/\zeta(s) = \begin{cases} e^{-ik(x'-x)} e^{k(\eta^{+'}-\eta^-+1)}, & \text{on the lower interface,} \\ e^{-ik(x'-x)} e^{k(\eta^{+'}-\eta^+)}, & \text{on the upper interface.} \end{cases} \tag{3.9}$$

Downloaded from https://www.cambridge.org/core. IP address: 18.222.167.249, on 16 Nov 2024 at 17:23:38, subject to the Cambridge Core terms of use, available at https://www.cambridge.org/core/terms. https://doi.org/10.1017/jfm.2024.73

Finally, we can obtain four boundary integral equations by taking the imaginary part of (3.5),

$$q_1(s') \sin(\theta^-(s')) = \underbrace{\frac{k}{\pi} \int_{-\alpha^-}^{\alpha^-} \operatorname{Im} \left( \frac{q_1(s)}{1 - \frac{\zeta(s')}{\zeta(s)}} \right) ds}_{\text{mirror image of lower interface}} - \underbrace{\frac{k}{\pi} \int_{-\alpha^-}^{\alpha^-} \operatorname{Im} \left( \frac{q_1(s)}{1 - \frac{\zeta(s')}{\zeta(s)}} \right) ds}_{\text{lower interface}}, \quad (3.10)$$

$$q_2^-(s') \sin(\theta^-(s')) = \underbrace{\frac{k}{\pi} \int_{-\alpha^-}^{\alpha^-} \operatorname{Im} \left( \frac{q_2^-(s)}{1 - \frac{\zeta(s')}{\zeta(s)}} \right) ds}_{\text{lower interface}} - \underbrace{\frac{k}{\pi} \int_{-\alpha^+}^{\alpha^+} \operatorname{Im} \left( \frac{q_2^+(s)}{1 - \frac{\zeta(s')}{\zeta(s)}} \right) ds}_{\text{upper interface}}, \quad (3.11)$$

$$q_2^+(s') \sin(\theta^+(s')) = \underbrace{\frac{k}{\pi} \int_{-\alpha^-}^{\alpha^-} \operatorname{Im} \left( \frac{q_2^-(s)}{1 - \frac{\zeta(s')}{\zeta(s)}} \right) ds}_{\text{lower interface}} - \underbrace{\frac{k}{\pi} \int_{-\alpha^+}^{\alpha^+} \operatorname{Im} \left( \frac{q_2^+(s)}{1 - \frac{\zeta(s')}{\zeta(s)}} \right) ds}_{\text{upper interface}}, \quad (3.12)$$

$$q_3(s') \sin(\theta^+(s')) = \underbrace{\frac{k}{\pi} \int_{-\alpha^+}^{\alpha^+} \operatorname{Im} \left( \frac{q_3(s)}{1 - \frac{\zeta(s')}{\zeta(s)}} \right) ds}_{\text{upper interface}} - \underbrace{\frac{k}{\pi} \int_{-\alpha^+}^{\alpha^+} \operatorname{Im} \left( \frac{q_3(s)}{1 - \frac{\zeta(s')}{\zeta(s)}} \right) ds}_{\text{mirror image of upper interface}}, \quad (3.13)$$

where  $2\alpha^-$  and  $2\alpha^+$  are the total arclength in a spatial period for the lower and upper interfaces,  $q_1$  and  $q_3$  are the tangential velocities of the lower and upper fluid layers on their corresponding interfaces,  $q_2^-$  and  $q_2^+$  are the tangential velocities of the middle fluid layer on the lower and the upper interfaces, and  $\theta^-$  and  $\theta^+$  are the inclination angles of the lower and upper interfaces. Note that we have put the point where  $s = 0$  on the symmetry axis, i.e. the  $y$ -axis.

### 3.2. Fourier series solutions

For the convenience of numerical calculation, we introduce two pseudoarclength parameters  $\tau^\pm = s/\alpha^\pm \in [-1, 1]$  and write the following Fourier series of the six unknown functions:

$$q_1 = \sum_{n=0}^{\infty} a_n \cos(n\pi\tau^-), \quad q_2^- = \sum_{n=0}^{\infty} b_n \cos(n\pi\tau^-), \quad q_2^+ = \sum_{n=0}^{\infty} c_n \cos(n\pi\tau^+), \quad (3.14a-c)$$

$$q_3 = \sum_{n=0}^{\infty} d_n \cos(n\pi\tau^+), \quad \theta^- = \sum_{n=1}^{\infty} e_n \sin(n\pi\tau^-), \quad \theta^+ = \sum_{n=1}^{\infty} f_n \sin(n\pi\tau^+). \tag{3.15a-c}$$

Using (3.4), we can construct the lower and upper interfaces from  $\theta^-$  and  $\theta^+$  by the following equations:

$$x^-(\tau^-) = \alpha^- \int_0^{\tau^-} \cos(\theta^-(\tau)) \, d\tau, \quad \eta^-(\tau^-) = \eta_0^- + \alpha^- \int_0^{\tau^-} \sin(\theta^-(\tau)) \, d\tau, \tag{3.16a,b}$$

$$x^+(\tau^+) = \alpha^+ \int_0^{\tau^+} \cos(\theta^+(\tau)) \, d\tau, \quad \eta^+(\tau^+) = \eta_0^+ + \alpha^+ \int_0^{\tau^+} \sin(\theta^+(\tau)) \, d\tau, \tag{3.17a,b}$$

in which  $\eta_0^\pm$  are unknowns. To guarantee spatial periodicity that  $x^\pm(\tau^\pm)|_0^1 = 2\pi/k$ , we must impose the following conditions:

$$\alpha^- \int_{-1}^1 \cos(\theta^-(\tau^-)) \, d\tau^- = \alpha^+ \int_{-1}^1 \cos(\theta^+(\tau^+)) \, d\tau^+ = \frac{2\pi}{k}. \tag{3.18}$$

To determine  $\eta_0^\pm$ , we need to impose the following constraints which represent volume conservation:

$$\int_0^1 \eta^- \frac{dx^-}{d\tau^-} \, d\tau^- = \int_0^1 \eta^+ \frac{dx^+}{d\tau^+} \, d\tau^+ = 0. \tag{3.19}$$

Also, we need to prescribe the current speed  $-c$  (which has been scaled to  $-1$ ) defined as the average velocity in the lower fluid

$$\frac{k}{2\pi} \int_{-\pi/k}^{\pi/k} u_1(x, y = \text{const.}) \, dx = -1, \tag{3.20}$$

where  $y = \text{const.}$  is an arbitrary horizontal line within the lower layer. Equation (3.20) can be rewritten in terms of  $q_1$  using the irrotationality condition

$$\frac{k}{2\pi} \int_{-\alpha^-}^{\alpha^-} q_1(s) \, ds = -1. \tag{3.21}$$

In addition, similar conditions for the middle and upper layers are also necessary. Here we focus on the case that all three layers have the same averaged background current (implying zero average shear between each layer). Therefore, the same condition as in (3.21) is adopted for  $q_2^-$ ,  $q_2^+$  and  $q_3$ . Using the pseudoarclength parameters, we have the following four conditions:

$$\frac{\alpha^- k}{2\pi} \int_{-1}^1 q_1 \, d\tau^- = \frac{\alpha^- k}{2\pi} \int_{-1}^1 q_2^- \, d\tau^- = \frac{\alpha^+ k}{2\pi} \int_{-1}^1 q_2^+ \, d\tau^+ = \frac{\alpha^+ k}{2\pi} \int_{-1}^1 q_3 \, d\tau^+ = -1. \tag{3.22}$$

These conditions imply the following equations:

$$a_0 = b_0 = -\frac{\pi}{\alpha^- k}, \quad c_0 = d_0 = -\frac{\pi}{\alpha^+ k}. \tag{3.23a,b}$$



*Nonlinear travelling periodic waves for the Euler equations*

3.3. *Newton’s method for the nonlinear system*

Since we focus on waves which have symmetry about the  $y$ -axis, only half of the spatial period is needed in the computation. Therefore, we introduce  $N$  uniformly distributed mesh points  $\tau_n^\pm$  in the right half-interval  $[0, 1]$ :

$$\tau_n^\pm = \frac{n-1}{N-1}, \quad n = 1, 2, \dots, N. \tag{3.24}$$

To avoid the singularity in the integral equations, we introduce a second set of mesh points  $\tau_n^{m\pm}$ :

$$\tau_n^{m\pm} = \frac{\tau_n^\pm + \tau_{n+1}^\pm}{2}, \quad n = 1, 2, \dots, N-1. \tag{3.25}$$

We let the boundary integral equations (3.10)–(3.13) to be satisfied on  $\tau_n^{m\pm}, n = 1, 2, \dots, N-1$ . The integrals are calculated by the trapezoid rule using the function values on  $\tau_n, n = 1, 2, \dots, N$ , which gives a spectral accuracy for periodic functions. The Bernoulli equations (2.4) and (2.5) are rewritten as

$$(q_2^-)^2 - R_1 q_1^2 + \frac{2(1-R_1)}{F^2} \left( -\frac{1}{2} + \eta^- \right) = B^-, \tag{3.26}$$

$$R_3 q_3^2 - (q_2^+)^2 + \frac{2(R_3-1)}{F^2} \left( \frac{1}{2} + \eta^+ \right) = B^+, \tag{3.27}$$

and satisfied on  $\tau_n, n = 1, 2, \dots, N$ . Together with the four conditions (3.18), (3.19), we have  $6N$  equations to solve. To close the system, we truncate the Fourier series after  $N$  terms to get  $6(N-1)$  unknown coefficients  $a_n, b_n, c_n, d_n, e_n, f_n (n = 1, 2, \dots, N-1)$  and six unknown constants  $B^+, B^-, \alpha^-, \alpha^+, \eta_0^-$  and  $\eta_0^+$ , which makes the number of unknowns  $6N$ .

This nonlinear system can be solved by Newton’s iteration. Initially, we choose a small-amplitude linear solution as the initial guess of iteration. The value of  $F$  is calculated from the dispersion relation. Once the iterations have converged to a small amplitude solution, we use continuation methods (usually with  $F$  as a continuation parameter) to compute the branch of solutions. To display the bifurcation curve clearly, we choose the wave speed  $F$  and a second parameter which measures the nonlinearity of the solutions. The wave amplitude is a candidate as usual, however, considering there are two interfaces and complex profiles, it is more appropriate to choose the wave energy  $E$  as the second parameter. It is given by

$$\begin{aligned} E = & -\frac{F^2 R_1}{2} \int_{-1}^1 \phi_1^s \frac{d\eta^-}{d\tau^-} d\tau^- + \frac{F^2}{2} \left( \int_{-1}^1 \phi_2^{-s} \frac{d\eta^-}{d\tau^-} d\tau^- - \int_{-1}^1 \phi_2^{+s} \frac{d\eta^+}{d\tau^+} d\tau^+ \right) \\ & + \frac{F^2 R_3}{2} \int_{-1}^1 \phi_3^s \frac{d\eta^+}{d\tau^+} d\tau^+ + \frac{R_1-1}{2} \int_{-1}^1 (\eta^-)^2 \frac{dx^-}{d\tau^-} d\tau^- + \frac{1-R_3}{2} \int_{-1}^1 (\eta^+)^2 \frac{dx^+}{d\tau^+} d\tau^+, \end{aligned} \tag{3.28}$$

where  $\phi_1^s$  and  $\phi_2^{-s}$  are the potential functions of the lower and the middle fluid layers on the lower interface,  $\phi_2^{+s}$  and  $\phi_3^s$  are the potential functions of the middle and upper layer on the upper interface. Hereafter, the bifurcation curves will always be plotted on the  $(F, E)$  space.

$kH$	$C_s$ (S&Y)	$C_s$ (M&S)	$C_s$ (two-layer)	$C_s$ (three-layer)
0.1	1.0010433	1.001043327	1.001043327	1.001043327
0.3	1.0093851	1.009385147	1.009385147	1.009385147
0.5	1.0260381	1.026038075	1.026038075	1.026038075
0.7	1.0509243	1.050924313	1.050924313	1.050924313
0.9	1.0839603	1.083960270	1.083960271	1.083960271
1.10	1.125454	1.125454593	1.125454593	1.125454593
1.20	1.149904	1.149903889	1.149903889	1.149903889
1.30	1.177	1.177754503	1.177754503	1.177754503
1.32	—	1.183901408	1.183901408	1.183901408
1.34	—	1.190327567	1.190327567	1.190327567
1.36	—	1.197125838	1.197125838	1.197125838
1.38	—	1.204514662	1.204514662	1.204514662
1.39	—	1.208645838	1.208645838	1.208645838
1.39	—	1.213326106	1.213326106	1.213326106
1.38	—	1.210675485	1.210675485	1.210675485
1.36	—	1.204401123	1.204401123	1.204401124
1.34	—	1.197369928	1.197369928	1.197369928
1.32	—	1.189740717	1.189740717	1.189740717
1.30	—	1.181506483	1.181506483	1.181506483
1.28	—	1.172510673	1.172510673	1.172510674

Table 1. Here  $C_s$  versus  $kH$  for two-layer interfacial gravity deep-water waves with density ratio 0.1. The second and third columns are results from Saffman & Yuen (1982) and Maklakov & Sharipov (2018). The results in fourth and fifth columns are calculated using the two-layer model in Guan *et al.* (2021a) and the current three-layer model with 500 Fourier modes.

The Boussinesq approximation is obtained by setting  $R_1 = R_3 = 1$  in the kinetic energy terms of the Bernoulli equations (3.26), (3.27) and the energy, resulting in

$$(q_2^-)^2 - q_1^2 + \frac{2(1 - R_1)}{F^2} \left( -\frac{1}{2} + \eta^- \right) = B^-, \tag{3.29}$$

$$q_3^2 - (q_2^+)^2 + \frac{2(R_3 - 1)}{F^2} \left( \frac{1}{2} + \eta^+ \right) = B^+, \tag{3.30}$$

$$E_b = -\frac{F^2}{2} \int_{-1}^1 \phi_1^s \frac{d\eta^-}{d\tau^-} d\tau^- + \frac{F^2}{2} \left( \int_{-1}^1 \phi_2^{-s} \frac{d\eta^-}{d\tau^-} d\tau^- - \int_{-1}^1 \phi_2^{+s} \frac{d\eta^+}{d\tau^+} d\tau^+ \right) + \frac{F^2}{2} \int_{-1}^1 \phi_3^s \frac{d\eta^+}{d\tau^+} d\tau^+ + \frac{R_1 - 1}{2} \int_{-1}^1 (\eta^-)^2 \frac{dx^-}{d\tau^-} d\tau^- + \frac{1 - R_3}{2} \int_{-1}^1 (\eta^+)^2 \frac{dx^+}{d\tau^+} d\tau^+. \tag{3.31}$$

## 4. Numerical results

### 4.1. Numerical accuracy

In table 1, we present the results of two-layer interfacial gravity waves previously obtained by Saffman & Yuen (1982) (second column), Maklakov & Sharipov (2018) (third column), Guan *et al.* (2021a) (forth column) and the results of current three-layer model (fifth column). By choosing  $R_1 = 10$ ,  $R_3 = 1$ ,  $h_1 = 100$ ,  $h_3 = 99$  and  $k = 1$ , we actually approach a two-layer interfacial deep-water wave setting whose effective density ratio

Nonlinear travelling periodic waves for the Euler equations

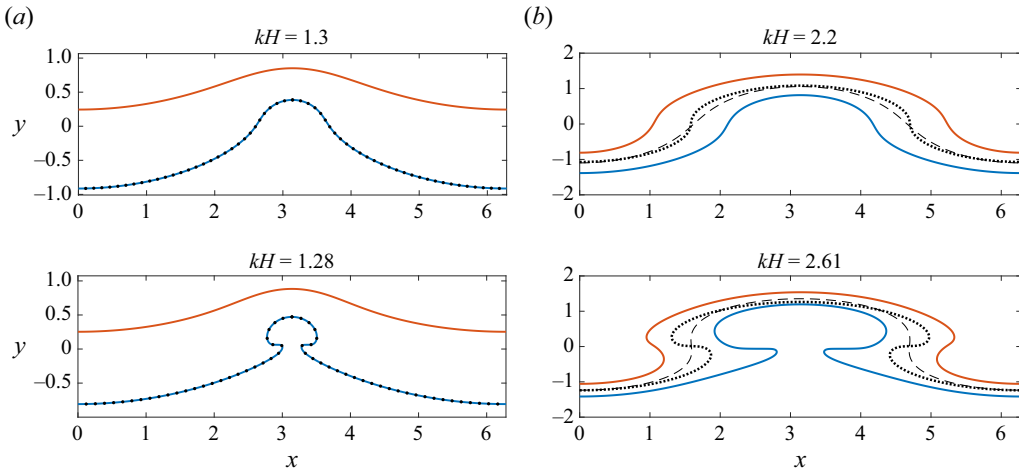


Figure 2. (a) Typical wave profiles of  $R_1 = 10$ ,  $R_3 = 1$ ,  $h_1 = 100$ ,  $h_3 = 99$  and  $k = 1$ . The upper and lower interfaces are the solid curves. Due to the chosen parameters, the upper curve is the real interface of a two-layer system and the lower curve is a streamline. The black dots are solutions of the corresponding two-layer deep water system with density ratio 0.1. (b) Typical wave profiles of  $R_1 = 1.01$ ,  $R_3 = .99$ ,  $h_1 = 99.5$ ,  $h_3 = 99.5$  and  $k = 1$ . The black dashed lines denote the mid streamlines of three-layer solutions. The black dots are solutions of the corresponding two-layer deep water system with density ratio 0.9802. In (a) and (b),  $H$  denotes the crest-to-trough wave amplitude of the blue curve.

is 0.1. The lower interface is still a real interface separating two different fluids, while the upper interface now becomes a streamline within the upper fluid. In table 1, we display the computed values of  $C_s$  for different given values of  $kH$ , where  $C_s$  is the dimensionless wave speed defined by Saffman & Yuen,  $k$  is the wavenumber and  $H$  is the wave amplitude defined as the difference between the displacement at the peak and the displacement at the trough. For this special deep-water case,  $C_s$  can be related to our  $F$  by the following relation:

$$C_s = F \sqrt{\frac{1 - R}{1 + R}}, \tag{4.1}$$

where  $R$  is the equivalent density ratio for the two-layer model and equals to 0.1 in this example. In our computations, we let  $N = 500$  to generate the results of three-layer model. Also, we recalculated the results of the corresponding two-layer model using the method in Guan *et al.* (2021a) with 500 Fourier modes. It is clear from the table that our three-layer result agrees with other authors' results in the first eight decimals for all wave amplitude using 500 Fourier modes, which shows that our algorithm has an excellent numerical accuracy. Two typical solutions with different given wave heights are shown in figure 2(a). We also plot solutions of the corresponding two-layer deep water system with density ratio 0.1 (black dots) for comparison. Furthermore, we compare the current three-layer model with the two-layer model in a different way. Following Rusås & Grue (2002), we choose  $R_1 = 1.01$  and  $R_3 = 0.99$  so that they satisfy  $R_1 + R_3 = 2$ , i.e. the middle layer has the mean density of the other two layers. We let  $h_1 = h_3 = 99.5$  to approximate the deep water condition. Due to the thinness of middle layer, one can assume that this whole layer can be represented by a typical streamline, for example, the middle one. Two typical wave profiles are plotted in figure 2(b), as well as the middle streamline (black dashed lines). To compare with these solutions, we choose the density ratio of the two-layer model to be  $0.9802 \approx 0.99/1.01$ . Two wave profiles are plotted with black dots. It should

Downloaded from https://www.cambridge.org/core. IP address: 18.222.167.249, on 16 Nov 2024 at 17:23:38, subject to the Cambridge Core terms of use, available at https://www.cambridge.org/core/terms. https://doi.org/10.1017/jfm.2024.77

be pointed out that there is no unique way to determine which solution of the two-layer model corresponds to the chosen three-layer solution. Matching the crest-to-trough height is not always possible, for example, the streamline plotted in the lower subpanel of 2(b) has larger crest-to-trough height than all the two-layer solutions with density ratio 0.9802. Therefore, we choose the solution of the two-layer model in an *ad hoc* way so that it measures the mean shape of the top and bottom interface well. It should be noted that the agreement between the dashed line and the dotted line is not good when the three-layer solution develops an overhanging profile, which means the basic assumption that the middle streamline resembles the two-layer solution breaks down. In fact, it is found that even for an overhanging solution, most streamlines are still non-overhanging except those very adjacent to the interface.

#### 4.2. Bifurcations and wave profiles

To clarify the bifurcation structures, we find that it is useful to compare the numerical solutions with the solutions obtained under the Boussinesq approximation. Hereafter we shall use the terms ‘Euler’ and ‘Boussinesq’ to distinguish the numerical solutions for the two systems when they appear in the same figure. Given the large parameter space ( $R_1$ ,  $R_3$ ,  $h_1$ ,  $h_3$  and  $k$  are physical parameters) we will mainly restrict our attention to the symmetric configurations and density stratification cases, assuming that  $R_1 - 1 = 1 - R_3$  and  $h_1 = h_3$ . We shall also focus more on cases where the density contrasts are not large. With a symmetric choice of parameters and under the Boussinesq approximation, the equations have the symmetry about the midline of the channel referred to above, i.e. the upside-down symmetry we defined in the preceding section.

Starting with mode-1 waves, we find in the Euler case, two closely connected bifurcation branches which collapse onto one branch in the Boussinesq case. A typical example for  $R_1 = 1.1$ ,  $R_3 = 0.9$ ,  $h_1 = 1$ ,  $h_3 = 1$  and  $k = 1$  is shown in figure 3 where the branches of the Euler case and the Boussinesq case are shown. Given a solution in the Boussinesq case, we can construct another solution via operations (2.10). These either lead to the same solution with upside-down symmetry and a phase shift (symmetric branch) or a new solution without such symmetry (symmetry-breaking branch). In the latter case, the new solution and the given solution are mirror images having the same energy  $E$ . The bifurcation diagram for the Boussinesq case has one symmetric branch and one symmetry-breaking branch which bifurcates near  $F = 0.3845$  from the symmetric branch. The Boussinesq case is in excellent agreement with the Euler case when the energy is small. The difference between the Boussinesq and the Euler cases becomes significant when the wave energy is increased. The solutions in the Euler case do not have the upside-down symmetry, hence splitting the symmetry-breaking branch of the Boussinesq curve into two distinct curves which terminate at different points, where one of the interfaces touches itself. The branches of the Euler’s equations are shown by the blue and red curves in the figure.

In figure 3 we also display five typical profiles of solutions to the Euler equation along the two branches. Solution (i) is almost upside-down symmetric (with a phase shift), while solution (ii) has developed some asymmetry. Solutions of the Boussinesq case with the same values of  $F$  are also plotted in figure 3(b) by the black dots. Solutions (i) of the Euler case and Boussinesq case are almost indistinguishable, while solutions (ii) exhibit some slight differences as expected because solutions in the Boussinesq case are always upside-down symmetric. The three almost limiting waves (iii), (iv) and (v) also do not exhibit upside-down symmetry although (iv) and (v) are approximately mirror images, as they are close to the symmetry-breaking Boussinesq bifurcated branch. As in

*Nonlinear travelling periodic waves for the Euler equations*

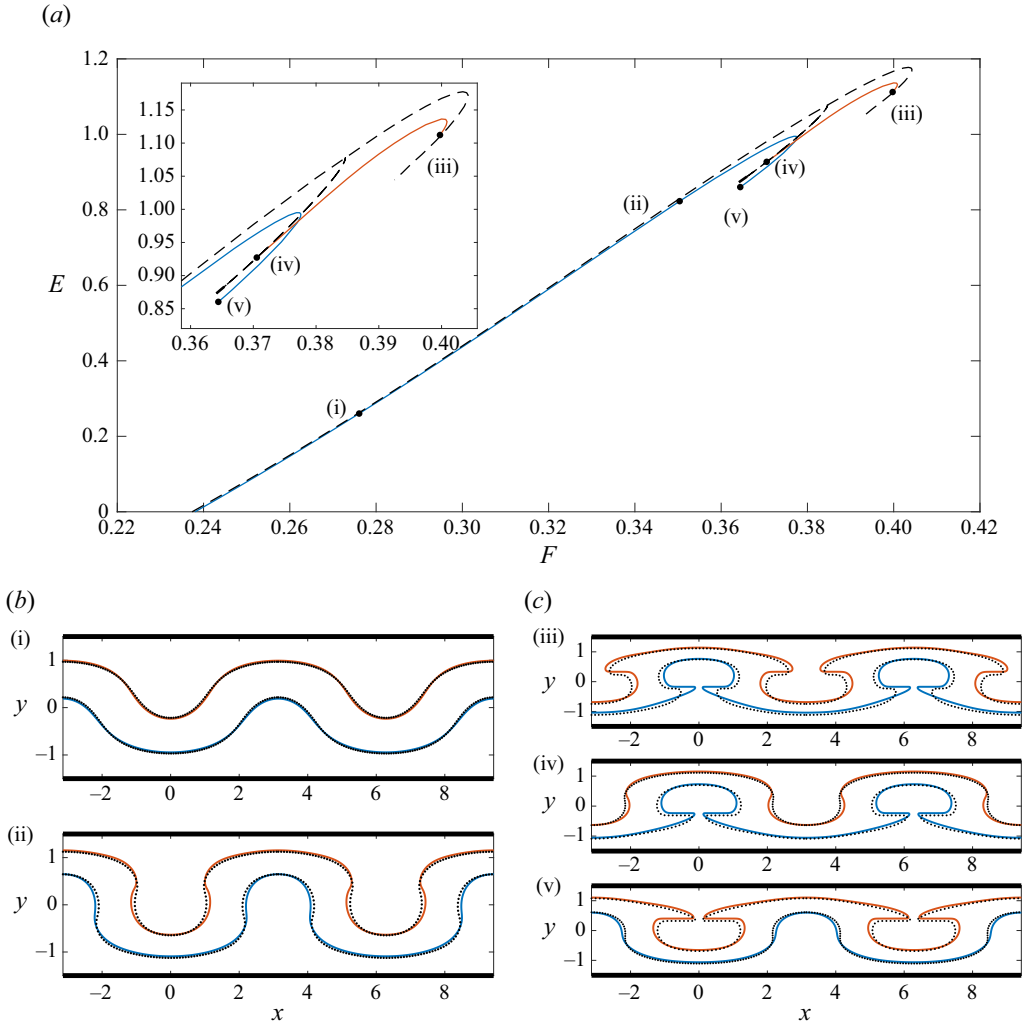


Figure 3. Numerical solutions of mode-1 waves with  $R_1 = 1.1$ ,  $R_3 = 0.9$ ,  $h_1 = 1$ ,  $h_3 = 1$ ,  $k = 1$ . (a) Speed–energy bifurcation curves: solid curves (Euler), dashed curves (Boussinesq). (b,c) Typical solutions of the Euler (solid lines) and Boussinesq (dotted lines) cases labelled in (a) plotted at the same value of the Froude number. In (bi,ii) and (ciii) the Boussinesq solutions are invariant under the transformation (2.10) (plus a phase shift of half a wavelength). In (civ) and (cv) the symmetry-breaking bifurcation means that solutions obtained by the transformation (2.10) are distinct.

the two-layer interfacial gravity wave case (Guan *et al.* 2021a), the mode-1 waves also feature overhanging profiles and self-intersecting singularities when the wave energy is sufficiently large. From the almost limiting waves (iii), (iv) and (v), it is reasonable to expect that their limiting waves would develop closed fluid bubbles on one of the interfaces and form a sharp angle at the intersection points. Using a local asymptotic analysis, one can show that it is possible for the interface to develop a  $120^\circ$  angle in contact with a closed fluid bubble (Guan *et al.* 2021b). In figure 4, a local blow-up of the almost limiting profiles (iii) of figure 3 is shown, as well as two dashed lines placed at  $120^\circ$  to each other.

For mode-2 waves, more than two bifurcation branches are usually found, which increases the complexity of the bifurcation structure. An example is shown in figure 5.

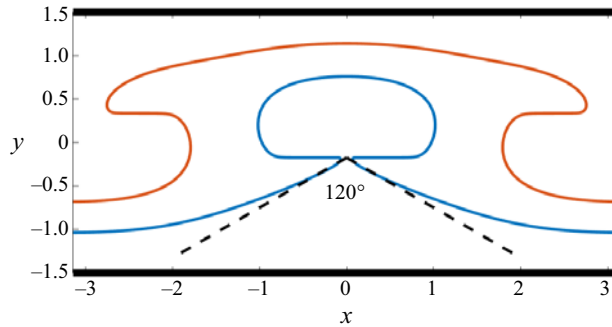


Figure 4. Almost limiting wave profile in figure 3(cii) in one spatial period. The black dashed line represents the limiting  $120^\circ$  angle.

The corresponding parameters are  $R_1 = 1.01$ ,  $R_3 = 0.99$ ,  $h_1 = 1$ ,  $h_3 = 1$  and  $k = 1.5$ . In figures 5(a) and 5(b), we plot the energy–speed bifurcation curves of the Euler case and the Boussinesq case, respectively. Due to the weak density stratification, the Boussinesq case displays an excellent agreement with the Euler case, with almost indistinguishable bifurcation curves. There are now two symmetry-breaking bifurcation points ( $F$  approximately 0.054 and 0.068) on the symmetric Boussinesq branch (blue) and two folded symmetry-breaking branches (red and yellow) grow from these points. Solutions (i) to (iv) in figure 5(c) are the almost symmetric solutions which can be seen both from their profiles and the fact that they lie near the symmetric branch of the Boussinesq approximation. On the other hand, solutions (v) to (viii) are almost limiting profiles of the symmetry-broken waves. It is interesting to note that these solutions show some characteristics of mode-1 waves, which is probably due to the mode-resonance mechanism described below. Like the mode-1 waves, we also expect the corresponding limiting waves to have closed bubbles attached to  $120^\circ$  angles. Solutions (iv), (vii) and (viii) are the almost limiting waves of this type. However, there are other possible limiting waves as solutions (v) and (vi) suggest. Taking solution (v) for example, one can infer that the upper interface (red) becomes self-intersecting if the local peak ( $x \approx \pm 0.8$ ) touches the mushroom’s base. In this fashion, there will be two closed fluid bubbles (of the upper fluid) which are symmetric with respect to the vertical lines  $x = 0$ . A further discussion on this new limiting configuration is beyond the scope of the current paper and shall not be addressed here.

For longer periodic mode-2 waves ( $k$  decreasing) the complexity of the bifurcation curves increases as there is the possibility of important resonances between the mode-2 waves and the mode-1 waves. Analogous to the well-known case of Wilton ripples in capillary–gravity surface waves (Wilton 1915), it is possible to find two wavenumbers  $k_1$  and  $k_2$  such that

$$c_{p1}(k_1) = c_{p2}(k_2), \quad mk_1 = nk_2, \quad n > m \text{ are two positive integers}, \quad (4.2)$$

where  $c_{p1}(k_1)$  is the phase speed of the mode-1 waves for  $k = k_1$  and  $c_{p2}(k_2)$  is the phase speed of the mode-2 waves for  $k = k_2$ . A similar mechanism has been pointed out by Chen & Forbes (2008) who focused on the case  $m = 1$ . These resonances can be seen from figure 6, where we plot the dispersion relation curves for  $R_1 = 1.1$ ,  $R_3 = 0.9$ ,  $h_1 = 1$  and  $h_3 = 1$ . For simplicity, we shall use the term  $(m, n)$  resonance to denote such conditions. Three examples corresponding to (1, 2), (1, 3) and (1, 10) are shown in figure 6 by the three dashed horizontal lines. There exist a countable number of resonant pairs since

*Nonlinear travelling periodic waves for the Euler equations*

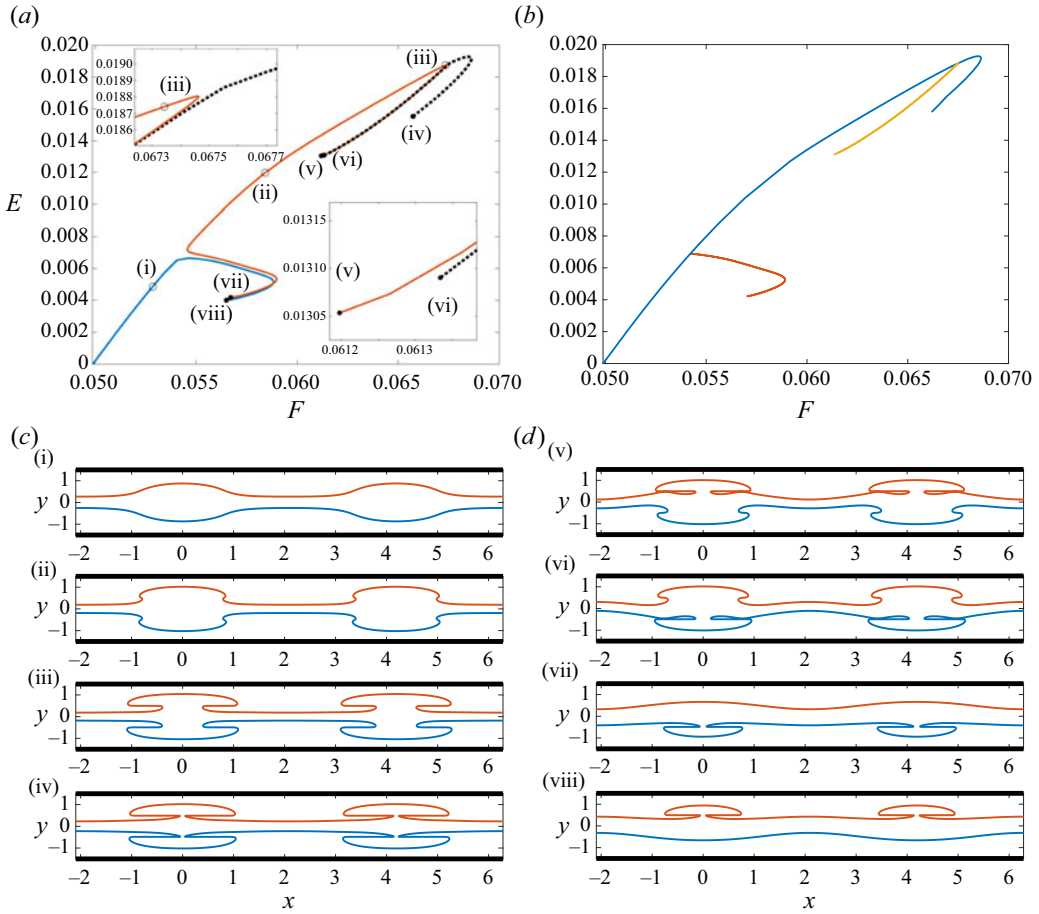


Figure 5. Numerical solutions of mode-2 waves with  $R_1 = 1.01$ ,  $R_3 = 0.99$ ,  $h_1 = 1$ ,  $h_3 = 1$ ,  $k = 1.5$ . (a) Speed–energy bifurcation branches of the Euler case. (b) Speed–energy bifurcation branches of the Boussinesq case. (c,d) Typical wave profiles of Euler case which are labelled in (a) and plotted in two spatial periods.

$n/m \rightarrow \infty$  when  $k_2 \rightarrow 0$ . These resonant pairs imply that if one chooses the wavenumber to satisfy (4.2), then, linearly, a mode-1 component and a mode-2 component coexist. This has consequences in the nonlinear solution branches.

In figure 7, we display the special example corresponding to the (1, 2) resonance of figure 6. In figure 7(a), the blue curve is the speed–energy bifurcation branch of solutions with  $k = 0.97651$  (which corresponds to one branch of Wilton ripple-like solution), and the black dashed curve is the speed–energy bifurcation mode-1 waves with  $k = 1.953$  for which the energy is calculated in two spatial periods. Solution (i), which is labelled by a black dot, is a small-amplitude linear wave, so we plot the corresponding upper interface (red) and lower interface (blue) in figure 7(b), respectively. In the bottom subpanel of figure 7(b), we plot  $|\hat{\theta}^-|$  versus  $n$  in a log-scale, where  $\hat{\theta}^-$  denotes the Fourier coefficient of the lower interfacial inclination  $\theta^-$ , and  $n$  is the order of the Fourier modes. It is clear that only the first two Fourier modes are significant while the rest are tiny enough to be neglected. Because of the existence of the resonant pair, the wave profile of (i) exhibits a mixture of the mode-1 and mode-2 waves. When the value of  $F$  increases,

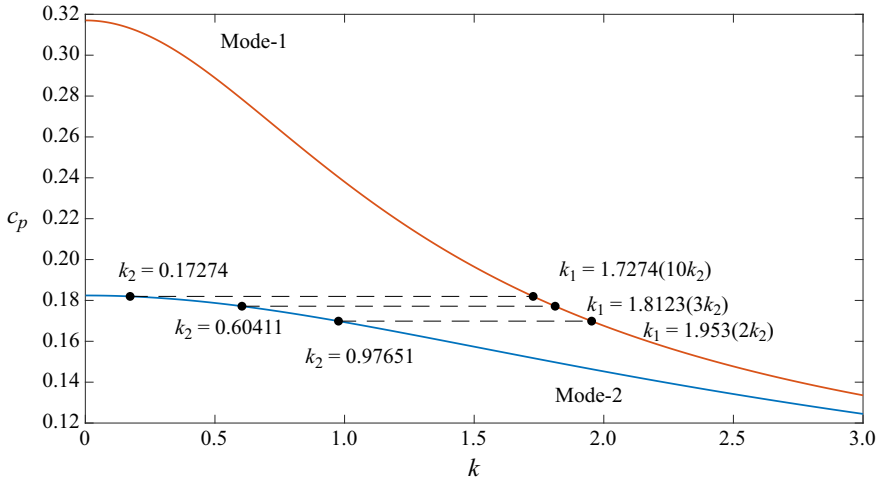


Figure 6. Dispersion relation curves with  $R_1 = 1.1, R_3 = 0.9, h_1 = 1$  and  $h_3 = 1$ . The upper and lower curves correspond to the mode-1 and mode-2 waves. The horizontal dashed lines represent three possible resonant pairs  $(k_1, k_2)$  for which  $k_1/k_2 = 2, 3, 10$ , respectively.

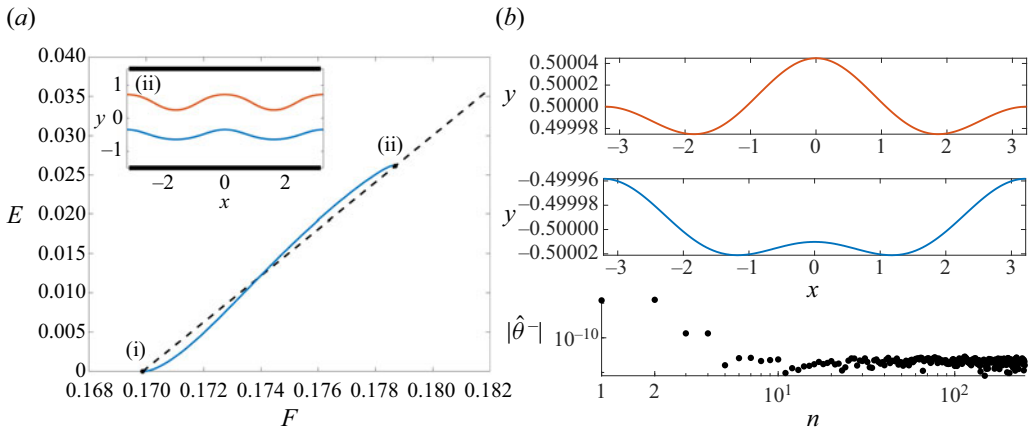


Figure 7. (a) Speed–energy bifurcation curves with  $R_1 = 1.1, R_3 = 0.9, h_1 = 1, h_3 = 1, k = 0.97651$  (blue, mode-2), and  $k = 1.953$  (black, mode-1). The energy of the mode-1 waves are calculated in two spatial periods. The figure in the inset box shows the wave profile of solution (ii). (b) The top and middle subpanels are the upper and lower interfaces of solution (i) in (a). The bottom subpanel displays the absolute value of  $\hat{\theta}^-$  of solution (i) in a log-scale, where  $\hat{\theta}^-$  is the Fourier coefficient of the lower interfacial inclination angle  $\theta^-$ , and  $n$  is the order of the Fourier modes.

the energy monotonically grows until the mode-2 wave bifurcation curve intersects the mode-1 wave bifurcation curve near  $F = 0.1787$ . The final solution (ii) is a mode-1 wave and is shown in the inset in figure 7(a). In general, this mode resonance still exists when  $k_1/k_2$  is a rational number rather than just an integer. In this case, we expect to see  $n$  mode-1 wave components coexist with  $m$  mode-2 waves, at least in the linear region. Figure 8 displays an example with parameters:  $R_1 = 1.01, R_3 = 0.99, h_1 = 1, h_3 = 1$  and  $k = 0.2525$ . According to the dispersion relation, the  $(2, 7)$  resonance is predicted when  $k_1 \approx 1.7679$  and  $k_2 \approx 0.5051$ . Therefore, we choose the length of the computing domain to support two mode-2 waves with  $k = 0.5051$  or seven mode-1 wave with  $k = 1.7679$ . Three



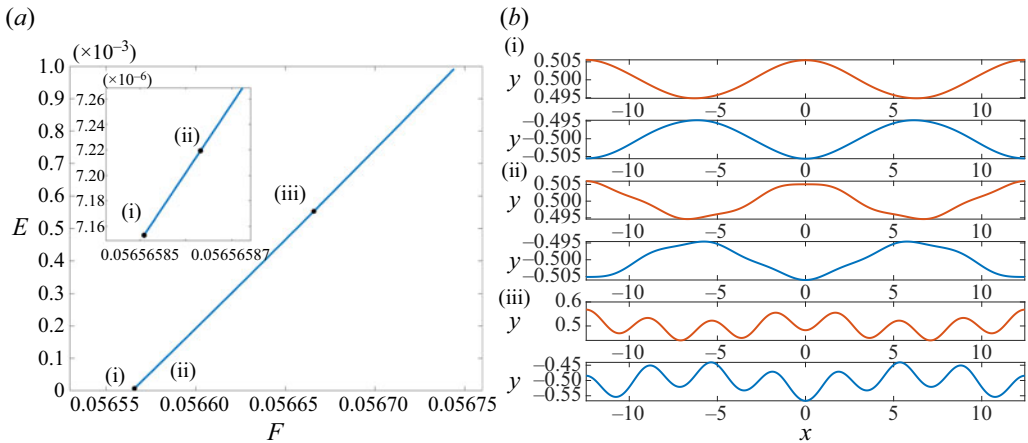


Figure 8. (a) Speed–energy bifurcation curves with  $R_1 = 1.01$ ,  $R_3 = 0.99$ ,  $h_1 = 1$ ,  $h_3 = 1$  and  $k = 0.2525$ . (b) Three typical wave profiles corresponding to the labelled solutions in (a). The red and blue curves are the upper and lower interfaces.

typical solutions are labelled on the local energy–speed bifurcation curve in figure 8(a), their wave profiles are plotted in figure 8(b). As the figure clearly shows, solution (i) is almost a standard mode-2 wave having two spatial periods. Solution (ii) has already generated some mode-1 components and clearly lost the double periodicity. Solution (iii) almost becomes a mode-1 wave and develops seven quasiperiodic mode-1 waves.

In fact, due to the nonlinearity, the resonant condition (4.2) only needs to be satisfied approximately to support the resonance. In figure 9, we plot six speed–energy bifurcation branches of the mode-2 waves with  $R_1 = 1.1$ ,  $R_3 = 0.9$ ,  $h_1 = 1$ ,  $h_3 = 1$  and  $k = 1$ . The black dashed lines are the speed–energy bifurcation curve of the mode-1 waves with  $k = 2$ . The blue curve and part of the red curve are of the (1, 2) resonant type. The wave profiles of solutions (i) and (ii) are shown in the two insets. This clearly indicates that they become the mode-1 waves with wavenumber  $k = 2$ . Nine almost limiting wave profiles are shown in figure 10. Note that the blue curve is not the only one which intersects the mode-1 bifurcation curve, the cyan branch also has an intersection at solution (x). The corresponding profile is a rather nonlinear mode-1 wave with an overhanging upper interface. This means that the mode-resonance exists not only in the weakly nonlinear region but also when solutions become highly nonlinear. Solutions (v) to (ix) are similar to those shown in figure 5. However, solutions (iii), (iv) and (xi) suggest the existence of a new limiting wave, but we shall not discuss it in the current paper.

An important question is how the bifurcation structure and wave profiles change when the five related parameters  $R_1$ ,  $R_3$ ,  $h_1$ ,  $h_3$  and  $k$  are gradually varied. In general, if we change the depth  $h_1$  and  $h_3$  but keep the other parameters fixed, the bifurcation structures and solutions are quantitatively similar. Wave profiles become spatially longer (shorter) if the depth is increased (decreased). On the other hand, if we gradually change the values of  $R_1$  and  $R_3$  away from the weak density stratification, but keep  $(R_1 - 1)/(1 - R_3)$  constant, i.e. the lower and the upper layer have the same density variation to the density of the middle layer, then one generally observe that the adjacent solution branches gradually get farther away from each other in the speed–energy bifurcation space. In figure 11, we display two numerical results with  $h_1 = h_3 = 1$ ,  $k = 1$ ,  $R_1 = 1.3$ ,  $R_3 = 0.7$  (figure 11a) and  $R_1 = 1.5$ ,  $R_3 = 0.5$  (figure 11b). For these two cases, the bifurcation

Downloaded from https://www.cambridge.org/core. IP address: 18.222.167.249, on 16 Nov 2024 at 17:23:38, subject to the Cambridge Core terms of use, available at https://www.cambridge.org/core/terms. https://doi.org/10.1017/jfm.2024.75

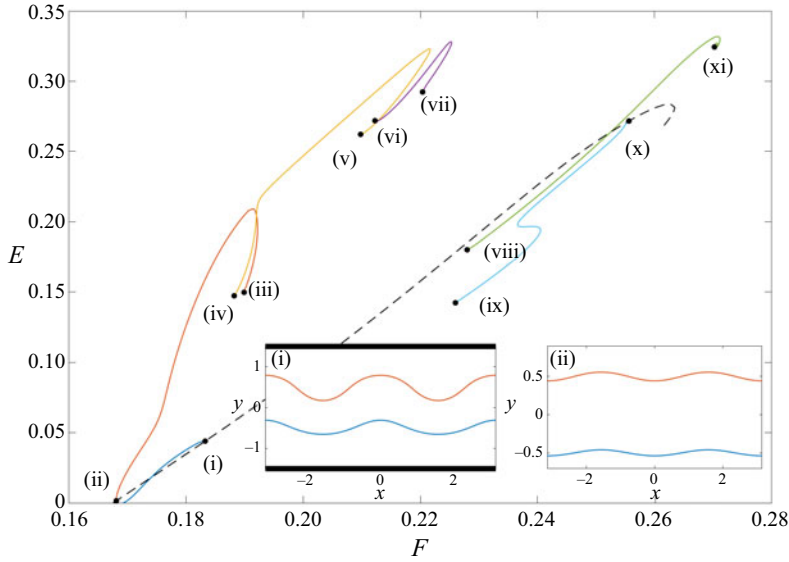


Figure 9. Energy–speed bifurcation curves and two related wave profiles of the mode-2 solutions with  $R_1 = 1.1$ ,  $R_3 = 0.9$ ,  $h_1 = 1$ ,  $h_3 = 1$  and  $k = 1$ . Associated (almost) limiting waves are labelled by black dots on curves. The black dashed line is the energy–speed bifurcation of the mode-1 solutions for the same values of  $R_1$ ,  $R_3$ ,  $h_1$ ,  $h_3$  and  $k = 2$  whose energy is calculated in two spatial periods. The two insets show the wave profiles corresponding to (i) and (ii).

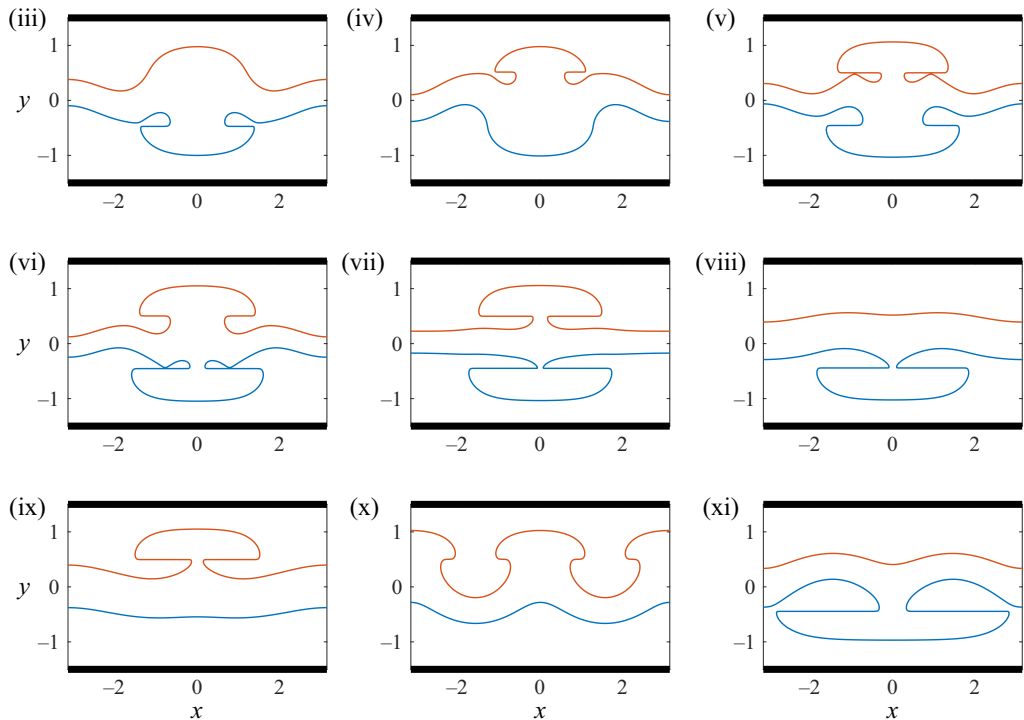


Figure 10. Almost limiting wave profiles corresponding to the nine labelled solutions (iii) to (xi) in figure 9.

*Nonlinear travelling periodic waves for the Euler equations*

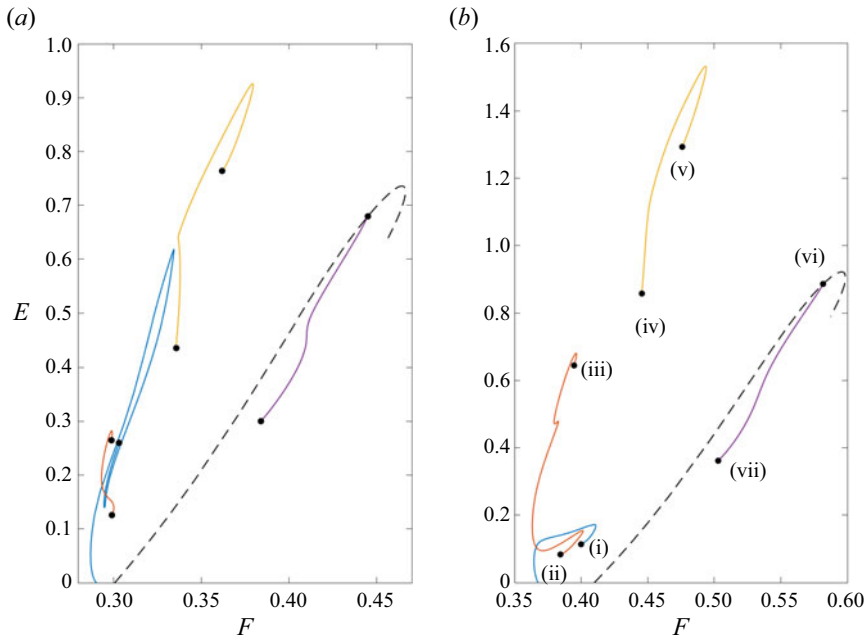


Figure 11. (a) Speed–energy bifurcation curves of the mode-2 waves with  $R_1 = 1.3, R_3 = 0.7, h_1 = 1, h_3 = 1$  and  $k = 1$ . (b) Speed–energy bifurcation curves of the mode-2 waves with  $R_1 = 1.5, R_3 = 0.5, h_1 = 1, h_3 = 1$  and  $k = 1$ . The black dashed curve is the bifurcation of the mode-1 waves with the same parameters except  $k = 2$ . The corresponding energy is calculated in two spatial periods.

structure is complex and the Boussinesq approximation is no longer valid since the density stratification is no longer weak. Comparing the bifurcations and the almost limiting wave profiles displayed in figure 12 with the numerical results shown in figures 9 and 10, it is noted that the number of bifurcation branches is decreased to four and some typical solutions in figure 10 vanish. In fact, this was also found in the two-layer interfacial waves that some bifurcation branches gradually shrink and ultimately disappear in the bifurcation space when the related parameters are varied (Guan *et al.* 2021a). Note that the (1, 2) resonance exists when  $k \approx 1.1$  for  $R_1 = 1.3, R_3 = 0.7$  and when  $k \approx 1.43$  for  $R_1 = 1.5, R_3 = 0.5$ . Therefore, we do not directly observe the mode-resonant phenomenon for these two cases since the wavenumbers that we choose is not very close to these critical wavenumbers. However, solutions (i), (ii) and (iii) still display some characteristics of resonance and can be thought of as the nonlinear evolution of mode resonance. The waves in figure 12 show that the possible limiting configurations are either a closed bubble attached to a  $120^\circ$  angle, or two closed bubbles located symmetrically to the vertical line  $x = 0$ , or special mode-1 waves having larger wavenumber. It is interesting to note that the almost closed bubble on the upper interface could have both upward and downward orientations.

If we fix the values of  $R_1, R_3, h_1$  and  $h_3$ , but gradually decrease  $k$ , then we obtain a family of long waves which converges to generalised solitary waves. In this process, the bifurcation structure becomes even more complex since there emerge a number of new resonant pairs. In figures 13–15, we exhibit the numerical solutions for  $R_1 = 1.01, R_3 = 0.99, h_1 = 1, h_3 = 1$  and  $k = 0.096$ . According to the linear theory, we can predict the critical values of  $F$  at which the mode-resonance occurs:

$$F = c_{p1}(nk), \quad n \text{ is a positive integer,} \quad (4.3)$$

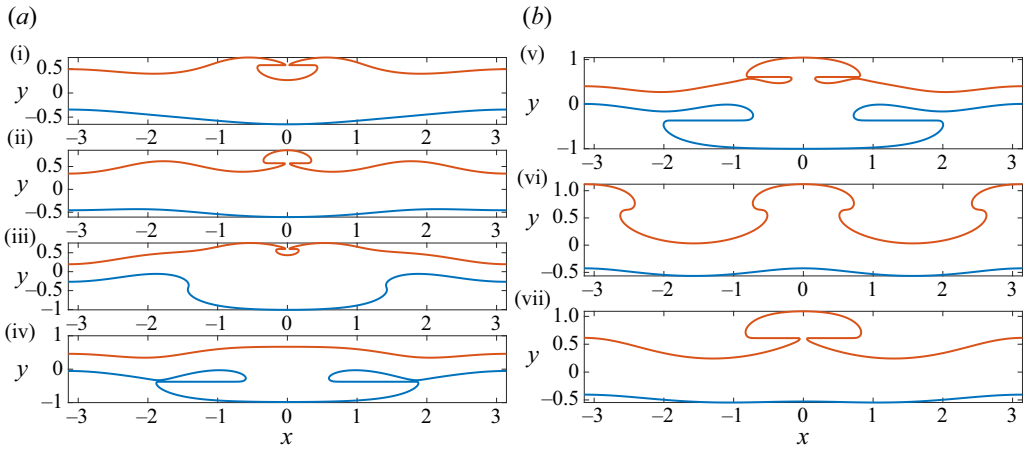


Figure 12. Almost limiting wave profiles corresponding to the labelled solutions (i) to (vii) in figure 11.

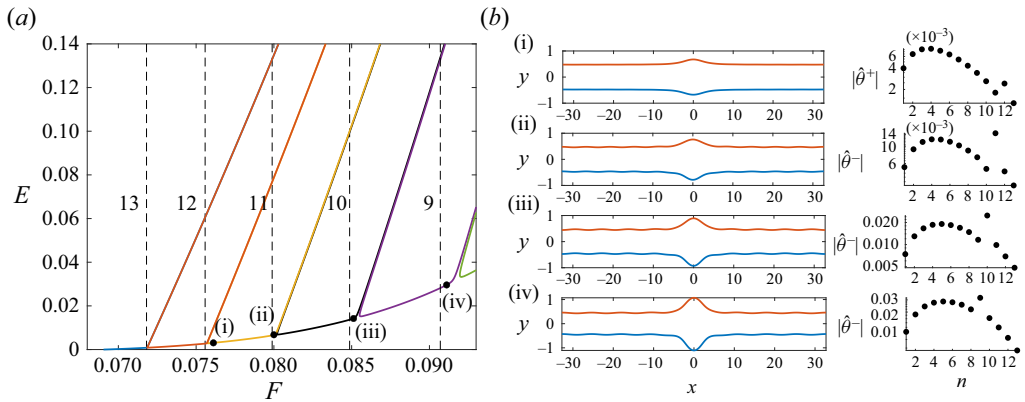


Figure 13. (a) Speed–energy bifurcation curves for  $R_1 = 1.01$ ,  $R_3 = 0.99$ ,  $h_1 = 50$ ,  $h_3 = 50$  and  $k = 0.096$ . The vertical dashed lines denote the predicted value of  $F$  where the mode-2 waves are resonant with the mode-1 waves having waves number  $nk$ . The corresponding values of  $n$  are shown close to the vertical lines. (b) Typical wave profiles and related absolute value of one of  $\hat{\theta}^\pm$  of the labelled solutions (i) to (iv) in (a), where  $\hat{\theta}^-$  and  $\hat{\theta}^+$  are the Fourier coefficients of the inclination angle of the lower and upper interface.

where  $c_{p1}(k)$  is the phase velocity of the mode-1 waves with wavenumber  $k$ . In figure 13(a), five critical values of  $F$  corresponding to  $n = 9$  to 13 are shown by the five vertical dashed lines. To show the existence of the resonant mode-1 component, we select four typical solutions in the region close to the predicted critical values of  $F$ , display their profiles, as well as the corresponding  $|\hat{\theta}^\pm|$  in a log-scale, where  $\hat{\theta}^\pm$  are the Fourier coefficients of the inclination angles of the upper and lower interfaces. It is interesting to note that this prediction gives fairly good agreement with the numerical results. More importantly, it indicates that close to these critical values there are new bifurcation branches. Therefore, the bifurcation structure is like a comb. Every branch has a part that belongs to the almost symmetric branch, and the symmetry-breaking part becomes a tooth of the comb at some turning points close to the predicted critical values of  $F$ . The second part of the whole bifurcation is shown in figure 14 as well as the four predicted critical values of  $F$  corresponding to  $n = 5$  to 8. As can be clearly seen, the positions of these turning points

### Nonlinear travelling periodic waves for the Euler equations

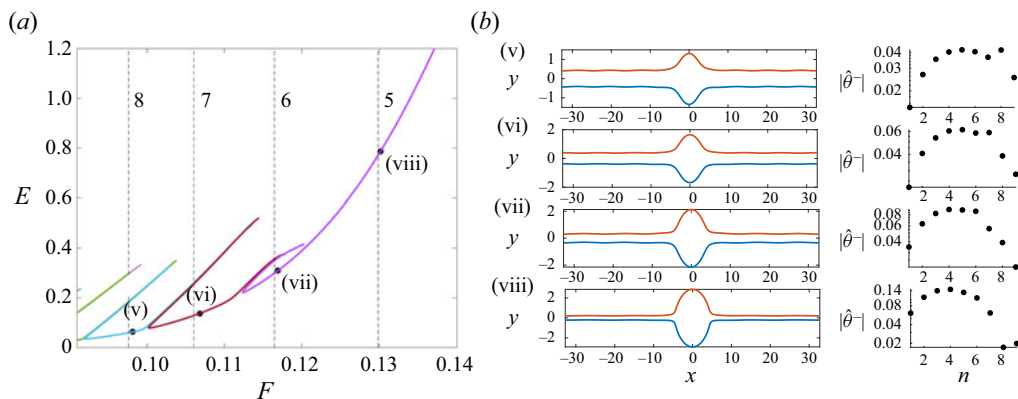


Figure 14. (a) Continuation of figure 13(a). (b) Typical wave profiles and related absolute value of  $\hat{\theta}^-$  of the labelled solutions (v) to (viii) in (a).

gradually differ from the predictions when waves become nonlinear, and the solutions gradually develop profiles of typical mode-2 generalised solitary wave type. The  $|\hat{\theta}^-|$  plot does not clearly show the resonant mode-1 component since more Fourier modes come into play.

If we follow different comb-teeth bifurcation curves and let the energy increase, then the wave profiles could develop rather different limiting configurations. In figure 15, we show six typical highly nonlinear solutions following those branches shown in figures 13 and 14. From top to bottom, these solutions come from the (1, 12), (1, 10), (1, 9), (1, 8), (1, 7) resonance teeth, and the rightmost almost symmetric branch in figure 14(a), i.e. the lower magenta branch. It turns out solutions could become pure mode-1 waves as shown in figure 15(a), or the long mode-1 waves with a distorted midsection and periodic mode-1 tails shown in figure 15(b–d), or the long mode-2 waves with periodic mode-1 tails shown in figure 15(e, f).

Figure 16 shows bifurcation curves for  $R_1 = 1.01$ ,  $R_3 = 0.99$ ,  $h_1 = h_3 = 0.1$  and  $k = 0.1$ . Here, the middle-layer is deep relative to the upper and lower layer, and the wave is relatively long. The main central pulses of the resonant mode-2 waves in this case are found to be concave (that is, the upper interface is of depression, and the lower is of elevation). Note that in this case, the branches are found to cross the linear long-wave speed of mode-1, which for these parameters is given by  $F \approx 0.0316$ . This feature was also observed for mode-2 solitary waves (Barros *et al.* 2020; Doak *et al.* 2022), and indeed when the magenta branch exits the linear spectrum, the resulting solutions are true mode-2 solitary waves with no resonances (solution B in the figure). Although linear waves do not exist for speeds  $F > 0.0316$ , nonlinear mode-1 solitary and periodic waves do, and the other branches which exit the spectrum still have resonances with nonlinear mode-1 waves.

When  $R_1 - 1 \neq 1 - R_3$ , there exists a kind of ‘trapped waves’ solution as shown by the typical solutions in figure 17. The related parameters are  $R_1 = 1.01$ ,  $R_3 = 0.95$ ,  $h_1 = 1$ ,  $h_3 = 1$  and  $k = 1$ . According to the dispersion relation, a (1, 7) resonance exists when  $k \approx 0.98472$ . This explains the profile in figure 17(a) where seven oscillations are generated on the top interface in one spatial period. Surprisingly, there appears only one single wave on the lower interface. These waves are very similar to those previously obtained by Lewis, Lake & Ko (1974) and Chen & Forbes (2008). When the amplitude of the lower interface gradually increases, it develops a bell-shaped profile and the oscillations

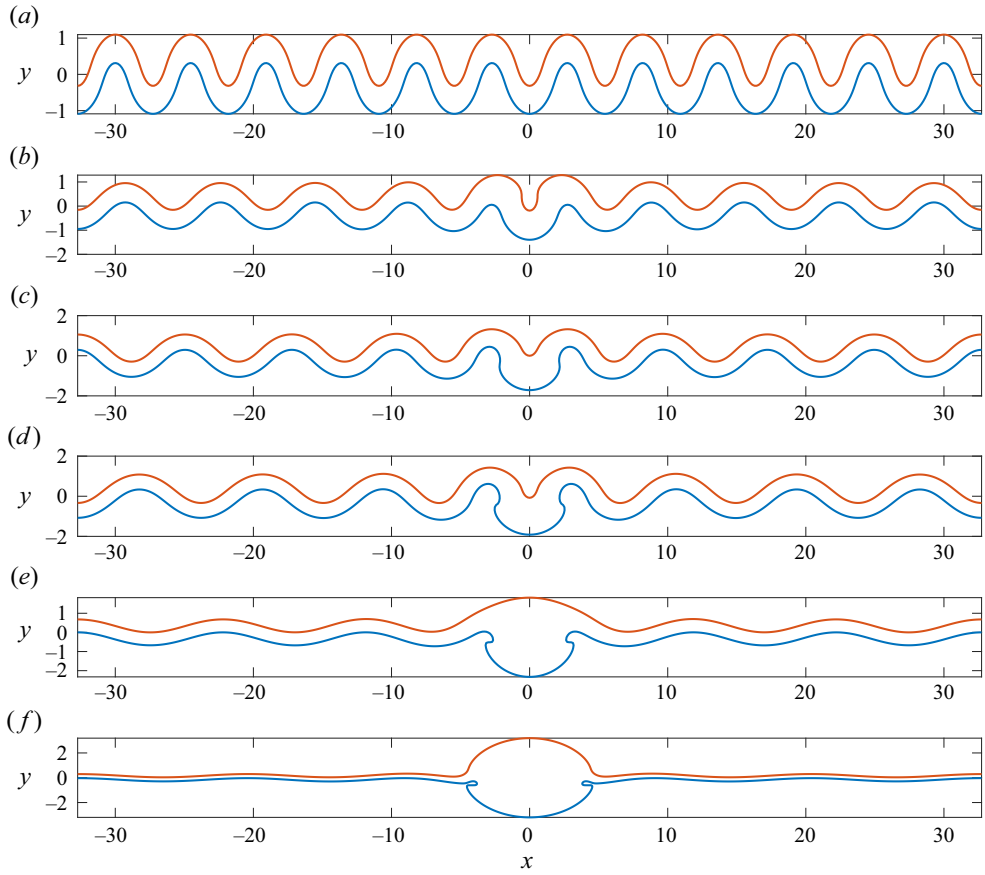


Figure 15. Six different (almost) limiting wave profiles with  $R_1 = 1.01$ ,  $R_3 = 0.99$ ,  $h_1 = 50$ ,  $h_3 = 50$  and  $k = 0.096$ .

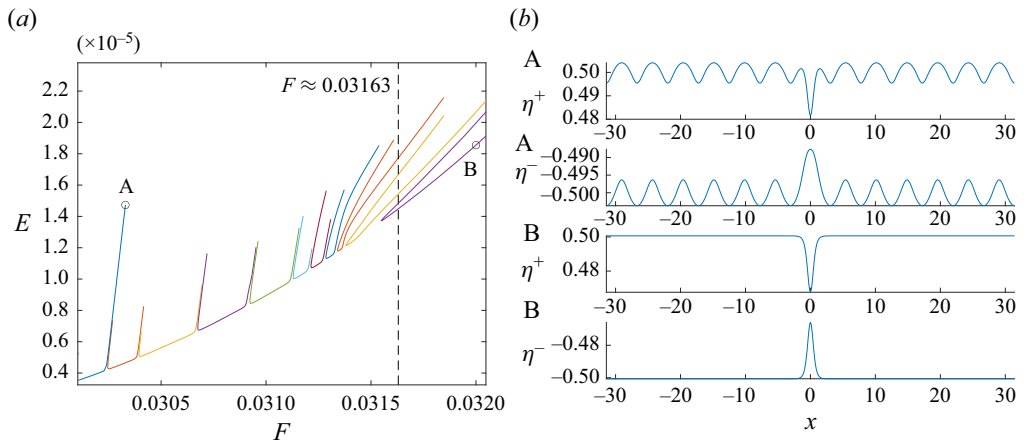


Figure 16. (a) Speed–energy bifurcations of mode-2 waves with  $R_1 = 1.01$ ,  $R_3 = 0.99$ ,  $h_1 = h_3 = 0.1$  and  $k = 0.1$ . The black dashed line represents the max phase speed of mode-1 waves. (b) Solutions A and B labelled in (a).

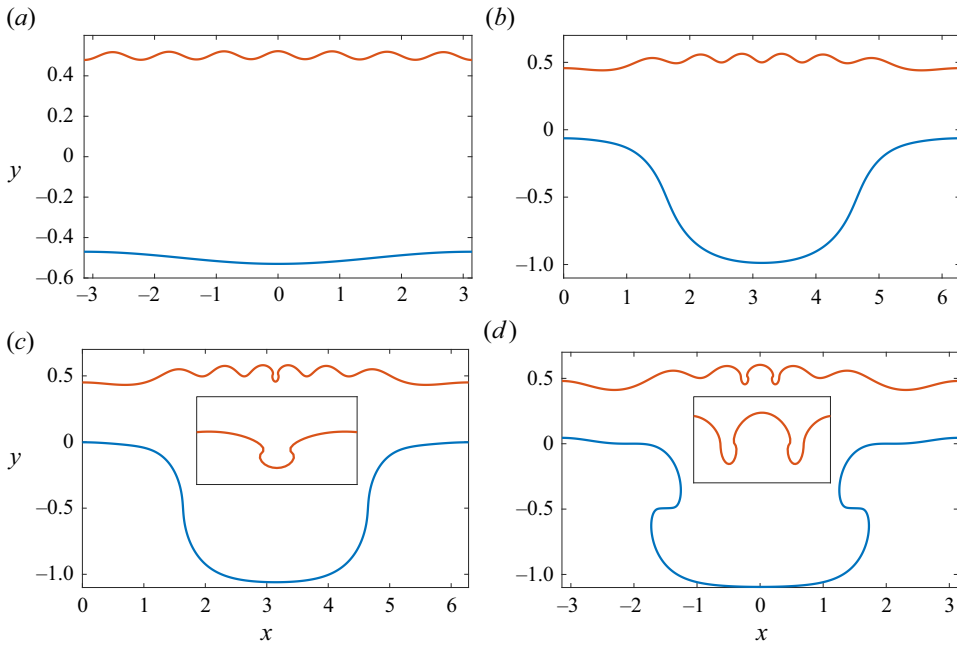


Figure 17. Four typical wave profiles with  $R_1 = 1.01$ ,  $R_3 = 0.95$ ,  $h_1 = 1$ ,  $h_3 = 1$  and  $k = 1$ .

on the upper interface gathered in the region above the trough of the lower interface. It is worth mentioning that similar solutions have been previously discovered in Liapidevskii & Gavrilov (2018) experimentally and in Doak *et al.* (2022) numerically. Figures 17(c) and 17(d) show that the waves could become even more nonlinear so that the upper interface develops an overhanging profile and tends to become self-intersecting. One or several closed bubbles are almost formed for solutions on different bifurcation branches. These overhanging structures are locally similar to those profiles shown before, except that the bubble size is greatly decreased. The lower interface also becomes steep and even overhanging. If the value of  $R_3$  is further decreased to zero, then the three-layer model approaches an ‘air–water–water’ setting. In this case, there are even more tiny oscillations on the upper interface and a large amplitude internal wave on the lower interface, which is a rough approximation of the real ‘surface–internal waves’ oceanic scenario.

### 5. Concluding remarks

In this paper, we present numerical calculations of periodic interfacial gravity waves in a three-layer fluid system. We assume that each layer has a finite depth and constant density, and impose two rigid lid conditions at the bottom and top (see figure 1). Density constants have non-increasing values from the bottom layer to top layer to ensure a statically stable configuration. Travelling wave solutions are calculated in a moving frame of reference where waves are steady. Using the analyticity of the complex velocity, we obtain four boundary integral equations from the Cauchy’s integral formula. Together with the Bernoulli equations and several other constraints imposed on the two interfaces, a nonlinear algebraic system is obtained and solved via Newton’s iteration. To achieve a high numerical accuracy, we apply the Fourier series technique. By setting the parameters to get an essentially two-layer deep water solution, we compare the wave speed for

Downloaded from https://www.cambridge.org/core. IP address: 18.222.167.249, on 16 Nov 2024 at 17:23:38, subject to the Cambridge Core terms of use, available at https://www.cambridge.org/core/terms. https://doi.org/10.1017/jfm.2024.77

different given wave heights with other authors' results and find an eight decimal-places accuracy. Using this algorithm, we explore the mode-1 and mode-2 wave solutions and find fruitful bifurcation structures. For clarity, we mainly focus on the weak stratification case for which the Boussinesq approximation is suited. Under this approximation, exactly symmetric solutions, which are invariant under the upside-down transformation, are found to form a symmetric solution branch. However, asymmetric solutions can coexist and their bifurcations connect to this symmetric branch. On the other hand, without using the Boussinesq assumption, solution branches are of a different nature, namely they are separated rather than connected (see [figure 3](#)), a sign of an imperfect bifurcation. For mode-1 waves, we observe one symmetry-breaking bifurcation, whereas for mode-2 waves we observe two. Limiting waves which are located at the endpoint of each branch show similar bubble–crest structure to those found in two-layer interfacial gravity waves. For mode-2 waves, more bifurcations and other possibilities of limiting waves are found. Among them, a mode-resonance mechanism is particularly interesting. Roughly speaking, this is similar to the well-known ‘Wilton ripple’ phenomenon in capillary–gravity waves. When the resonance condition (4.2) is satisfied, wave profiles can display a hybrid character of mode-1 and mode-2 waves because these modes have the same phase speed and thus coexist. Due to this mechanism, bifurcations can connect waves of different modes which results in a far more complicated structure than that of mode-1 waves (see [figure 9](#) for example). When density ratios are gradually changed and beyond the weak stratification region, we observe the separation of bifurcation curves that are gathered initially, as well as the distortion of related wave profiles (see [figures 12](#) and [17](#)). When we decrease the wavenumber to get a long wave approximation of generalised solitary waves, we find the comb-shaped bifurcation structure ([figures 13](#) and [14](#)). Following each tooth of the comb, we get generalised solitary waves having different numbers of periodic mode-1 tails. Surprisingly, these numbers can be well predicted by the resonant condition (4.2).

From a physical perspective, any finite-amplitude interfacial gravity wave suffers from the Kelvin–Helmholtz instability, making the layered-Euler equations mathematically ill-posed for time evolution. Without regularising effects, the instability grows unboundedly fast as the wavenumber increases. However, in real two-layer fluid configurations or fluids with a continuous sharp density stratification, the Kelvin–Helmholtz instability can be suppressed by the stratification profile or other effects, preventing the breakdown of large-scale wave motion (Chumakova *et al.* 2009a). Therefore, we can expect that stable solutions exist in a long-wave region (Chumakova *et al.* 2009b). Recently, Carr, Davies & Hoebbers (2015) observed stable mode-2 waves in their laboratory experiments. Some of the waves are very similar to our numerical solutions ([figure 5c](#)) and those in [figures 13](#) and [14](#). In addition, the experiments performed by Liapidevskii & Gavrillov (2018) suggest that the waves in [figure 17\(a,b\)](#) may be stable.

**Funding.** X.G. would like to acknowledge the support from the Chinese Scholarship Council (csc no. 202004910418). A.D. is funded by the EPSRC National Fellowship in Fluid Dynamics (EP/X028607/1).

**Declaration of interests.** The authors report no conflict of interest.

#### Author ORCIDs.

✉ Xin Guan <https://orcid.org/0000-0002-7594-4861>;

✉ Alex Doak <https://orcid.org/0000-0003-4718-6095>;

✉ Paul Milewski <https://orcid.org/0000-0003-4454-8441>.



REFERENCES

- AKYLAS, T.R. & GRIMSHAW, R. 1992 Solitary internal waves with oscillatory tails. *J. Fluid Mech.* **242**, 279–298.
- BARROS, R. & CHOI, W. 2011 Holmboe instability in non-Boussinesq fluids. *Phys. Fluids* **23** (12), 124103.
- BARROS, R., CHOI, W. & MILEWSKI, P.A. 2020 Strongly nonlinear effects on internal solitary waves in three-layer flows. *J. Fluid Mech.* **883**, A16.
- BOONKASAME, A. & MILEWSKI, P. 2012 The stability of large-amplitude shallow interfacial non-Boussinesq flows. *Stud. Appl. Maths* **128** (1), 40–58.
- CAMASSA, R., CHEN, S., FALQUI, G., ORTENZI, G. & PEDRONI, M. 2012 An inertia ‘paradox’ for incompressible stratified Euler fluids. *J. Fluid Mech.* **695**, 330–340.
- CARR, M., DAVIES, P.A. & HOEBERS, R.P. 2015 Experiments on the structure and stability of mode-2 internal solitary-like waves propagating on an offset pycnocline. *Phys. Fluids* **27** (4), 046602.
- CHEN, M.J. & FORBES, L.K. 2008 Steady periodic waves in a three-layer fluid with shear in the middle layer. *J. Fluid Mech.* **594**, 157–181.
- CHOI, W. & CAMASSA, R. 1999 Fully nonlinear internal waves in a two-fluid system. *J. Fluid Mech.* **396**, 1–36.
- CHUMAKOVA, L., MENZAQUE, F.E., MILEWSKI, P.A., ROSALES, R.R., TABAK, E.G. & TURNER, C.V. 2009a Shear instability for stratified hydrostatic flows. *Commun. Pure Appl. Maths* **62** (2), 183–197.
- CHUMAKOVA, L., MENZAQUE, F.E., MILEWSKI, P.A., ROSALES, R.R., TABAK, E.G. & TURNER, C.V. 2009b Stability properties and nonlinear mappings of two and three-layer stratified flows. *Stud. Appl. Maths* **122** (2), 123–137.
- DOAK, A., BARROS, R. & MILEWSKI, P.A. 2022 Large mode-2 internal solitary waves in three-layer flows. *J. Fluid Mech.* **953**, A42.
- EVANS, W.A.B. & FORD, M.J. 1996 An integral equation approach to internal (2-layer) solitary waves. *Phys. Fluids* **8** (8), 2032–2047.
- GRIMSHAW, R.H.J., PELINOVSKY, E. & TALIPOVA, T. 1997 The modified Korteweg - de Vries equation in the theory of large-amplitude internal waves. *Nonlinear Process. Geophys.* **4** (4), 237–250.
- GRIMSHAW, R.H.J. & PULLIN, D.I. 1986 Extreme interfacial waves. *Phys. Fluids* **29** (9), 2802–2807.
- GUAN, X., VANDEN-BROECK, J.-M. & WANG, Z. 2021a New solutions for periodic interfacial gravity waves. *J. Fluid Mech.* **928**, R5.
- GUAN, X., VANDEN-BROECK, J.-M., WANG, Z. & DIAS, F. 2021b A local model for the limiting configuration of interfacial solitary waves. *J. Fluid Mech.* **921**, A9.
- GUHA, A. & RAJ, R. 2018 On the inertial effects of density variation in stratified shear flows. *Phys. Fluids* **30** (12), 126603.
- HEIFETZ, E. & MAK, J. 2015 Stratified shear flow instabilities in the non-Boussinesq regime. *Phys. Fluids* **27** (8), 086601.
- JO, T.-C. & CHOI, Y.-K. 2014 Dynamics of strongly nonlinear internal long waves in a three-layer fluid system. *Ocean Sci. J.* **49** (4), 357–366.
- KURKINA, O.E., KURKIN, A.A., ROUVINSKAYA, E.A. & SOOMERE, T. 2015 Propagation regimes of interfacial solitary waves in a three-layer fluid. *Nonlinear Process. Geophys.* **22** (2), 117–132.
- LAMB, K.G. 2000 Conjugate flows for a three-layer fluid. *Phys. Fluids* **12** (9), 2169–2185.
- LEWIS, J.E., LAKE, B.M. & KO, D.R.S. 1974 On the interaction of internal waves and surface gravity waves. *J. Fluid Mech.* **63** (4), 773–800.
- LIAPIDEVSKII, V.Y. & GAVRILOV, N.V. 2018 Large internal solitary waves in shallow waters. In *The Ocean in Motion*, pp. 87–108. Springer.
- MAKLAKOV, D.V. & SHARIPOV, R.R. 2018 Almost limiting configurations of steady interfacial overhanging gravity waves. *J. Fluid Mech.* **856**, 673–708.
- MİYATA, M. 1988 *Long Internal Waves of Large Amplitude*, pp. 399–406. Springer.
- OSTROVSKY, L.A. & STEPANYANTS, Y.A. 2005 Internal solitons in laboratory experiments: comparison with theoretical models. *Chaos* **15** (3), 037111.
- RUSÅS, P.-O. 2000 On nonlinear internal waves in two- and three-layer fluids. PhD thesis, University of Oslo.
- RUSÅS, P.-O. & GRUE, J. 2002 Solitary waves and conjugate flows in a three-layer fluid. *Eur. J. Mech. (B/Fluids)* **21** (2), 185–206.
- SAFFMAN, P.G. & YUEN, H.C. 1982 Finite-amplitude interfacial waves in the presence of a current. *J. Fluid Mech.* **123**, 459–476.
- TURNER, R.E.L. & VANDEN-BROECK, J.-M. 1988 Broadening of interfacial solitary waves. *Phys. Fluids* **31** (9), 2486–2490.
- WILTON, J.R. 1915 On ripples. *Phil. Mag.* **29** (173), 688–700.
- YIH, C.-S. 2012 *Stratified Flows*. Elsevier.